Journal of Applied Physics ARTICLE pubs.aip.org/aip/jap

Ultrawide bandgap spinel γ-$(Ga_{0.8}Ge_{0.2})_2O_3$ alloy semiconductor epitaxial thin films

Cite as: J. Appl. Phys. **137**, 175302 (2025); doi: 10.1063/5.0255699
Submitted: 31 December 2024 · Accepted: 14 April 2025 ·
Published Online: 2 May 2025

Jingjing Yu,[1] Sijun Luo,[1,a)] Daniel Splith,[1] Susanne Selle,[2] Katrin Thieme,[2] Stephan Gierth,[2] Thorsten Schultz,[3,4] Peter Schlupp,[1] Chris Sturm,[1] Holger von Wenckstern,[1] Michael Lorenz,[1] Norbert Koch,[3,4] Thomas Höche,[2] and Marius Grundmann[1]

AFFILIATIONS

[1]Felix Bloch Institute for Solid State Physics, Faculty of Physics and Earth System Sciences, Universität Leipzig, 04103 Leipzig, Germany
[2]Fraunhofer Institute for Microstructure of Materials and Systems (IMWS), 06120 Halle, Germany
[3]Helmholtz-Zentrum Berlin für Materialien und Energie GmbH, 14109 Berlin, Germany
[4]Department of Physics, Humboldt-Universität zu Berlin, 12489 Berlin, Germany

[a)]**Author to whom correspondence should be addressed:** sijun.luo@physik.uni-leipzig.de

ABSTRACT

Epitaxial growth of phase-pure and high-quality spinel γ-Ga_2O_3-based semiconductor thin films has been a big challenge for fundamental research on metastable defective inverse spinel γ-Ga_2O_3 semiconductors in view of potential device application. We report experimental results on epitaxial growth, microstructural, and electrical transport properties of (001)-oriented nominal γ-$(Ga_{0.8}Ge_{0.2})_2O_3$ alloy semiconductor single crystal thin films with a coherent interface on cubic spinel (001) $MgAl_2O_4$ substrates by pulsed laser deposition using a Ge-rich target. Pristine films are found to be composed of about 2 nm thick insulating Ge-rich surface layers and the high-quality epitaxial n-type semiconductor film layers consisting of partially subvalent Ge^{2+} and Ga^{1+} cations as well as major components of normal Ge^{4+} and Ga^{3+} cations. Epitaxial films exhibit a direct bandgap of about 5.2 ± 0.1 eV and a valence band maximum of about 3.3 ± 0.1 eV below the Fermi level at room temperature. We further report a demonstration of γ-$(Ga_{0.8}Ge_{0.2})_2O_3$ thin film-based metal-semiconductor field-effect transistor (MESFET) with the PtO_x/Pt Schottky gate contact realized upon the surface pretreatment by Ar/O_2 plasma etching. The MESFET device exhibits a clear field-effect with drain current modulation of about 10^5 orders of magnitude. This work not only significantly advances the fundamental and application-oriented research on epitaxial spinel γ-Ga_2O_3-based semiconductor films for practical device application but also offers new insight into microstructural characteristics of ultrawide bandgap spinel oxide semiconductor epitaxial thin films.

I. INTRODUCTION

Metastable spinel γ-Ga_2O_3 is one of the five crystalline polymorphs of ultrawide bandgap semiconductor gallium oxides (Ga_2O_3).[1–3] The thermodynamically stable phase β-Ga_2O_3 has been well-studied in the forms of single crystals and thin films due to its great potential in semiconductor power electronics.[4–6] Recently, metastable defective spinel structure γ-Ga_2O_3 has attracted increasing research interest for its less clear microstructure and formations from phase transformations[7–15] and the high radiation tolerance for potential device application in harsh environments.[16,17] In the cubic defective inverse disordered spinel γ-Ga_2O_3 (space group Fd-3m, No. 227), there exist about one third of unoccupied octahedral sites for cations while the oxygen vacancies coexist to compensate the charges.[7,18] Normally phase-pure bulk single crystals and epitaxial thin films with a high crystal quality are preferable for the fundamental and application-oriented research for the purpose of potential device application; however, experimental results in growth and properties of bulk γ-Ga_2O_3 single crystals have not been reported yet.

Although undoped γ-Ga_2O_3 epitaxial thin films normally exhibit poor crystalline quality as well as impurity phase of β-Ga_2O_3, a relatively high doping content of about 7–8 cation %

Mn was first reported to stabilize the phase-pure (111)-oriented γ-Ga_2O_3 thin films epitaxially grown on (00.1) sapphire substrates by pulsed laser deposition (PLD),[19,20] and further found to give rise to the high-quality pseudocubic (001) Mn-doped γ-Ga_2O_3 epitaxial thin films with a coherent interface on cubic spinel (001) $MgAl_2O_4$ substrates by PLD.[21,22] In addition, high-quality (001)-oriented γ-$(Al_xGa_{1-x})_2O_3$ alloy thin films ($x \geq 0.22$) were also epitaxially grown on (001) $MgAl_2O_4$ substrates by plasma-assisted molecular beam epitaxy.[23] Whereas electrical properties of γ-$(Al_xGa_{1-x})_2O_3$ and Mn-doped γ-Ga_2O_3 epitaxial films were not reported. The first reported (to date the only available) conducting phase-pure γ-Ga_2O_3 epitaxial thin films were the (001)-oriented Si-doped γ-Ga_2O_3 thin films (with 0.24 cation % Si doping) epitaxially grown on (001) $MgAl_2O_4$ substrates by PLD.[24] But these poor-quality films show broad rocking curves of (004) reflection with large values of full width at half maximum of around 2.4°–3.0° and exhibit the degenerate n-type transport properties with temperature-independent Hall carrier concentration of $1.8–2.0 \times 10^{19}$ cm^{-3} and mobility of 1.6–0.9 $cm^2 V^{-1} s^{-1}$.[24] To date, the experimental results on field-effect transistors (FETs) of phase-pure γ-Ga_2O_3-based epitaxial thin films are not available.

A relatively high concentration of cationic doping or alloying combined with (001)-oriented $MgAl_2O_4$ single crystal substrates seems to be the key required for growing high-quality γ-Ga_2O_3 epitaxial thin films through a formation of atomic lattice matched coherent interface.[21–23] Ge is commonly considered a good dopant for n-type doping in Ga_2O_3.[25,26] In the cubic spinel heterostructural system of γ-Ga_2O_3 epitaxial thin films with $MgAl_2O_4$ substrates, the lattice mismatch is about 2.0% according to the reported bulk lattice constants of 8.24 Å (γ-Ga_2O_3) and 8.08 Å ($MgAl_2O_4$).[3,27] The empirical radii of four-coordinated and six-coordinated Ga^{3+} cations are 0.47 and 0.62 Å, respectively, in the tetrahedral and octahedral sites, which are a little greater than that of Ge^{4+} cations (0.39 and 0.53 Å).[28] Doping with the smaller Ge^{4+} cations would reduce the lattice mismatch between the films and substrates to easily form a lattice matched coherent interface. A major challenge in vapor deposition of epitaxial Ga_2O_3 thin films with high-concentration Ge doping or alloying to overcome is probably the large difference in vapor pressure between Ga and volatile Ge at high temperatures.[25,29] Recently, we found that using Zn-rich targets in PLD growth of epitaxial Zn-containing complex oxide thin films could compensate the serious loss of volatile Zn.[30,31] In this work, we report the heteroepitaxial growth, microstructural characteristics, and electrical transport properties of nominal γ-$(Ga_{0.8}Ge_{0.2})_2O_3$ alloy semiconductor thin films on cubic (001) $MgAl_2O_4$ substrates by PLD using a Ge-rich target made of 5 wt. % β-Ga_2O_3 and 95 wt. % GeO_2 raw powders (Ga: Ge atomic ratio of about 1:17).

To show the potential of γ-$(Ga_{0.8}Ge_{0.2})_2O_3$ alloy semiconductor epitaxial thin films for practical FETs device application, we further report the first demonstration of γ-Ga_2O_3 film-based metal-semiconductor field-effect transistors (MESFETs) by using the n-type γ-$(Ga_{0.8}Ge_{0.2})_2O_3$ alloy semiconductor thin film as a channel layer. It is worth mentioning that the first demonstration of single-crystal Ga_2O_3 transistors for practical power device applications was the n-channel β-Ga_2O_3 MESFETs reported in early 2012.[32] In this study, we fabricate and characterize n-channel γ-$(Ga_{0.8}Ge_{0.2})_2O_3$ film-based MESFETs. The oxidized Pt (PtO_x) layer is selected as the Schottky gate contact for MESFETs considering the increase in work function by about 1.0 ± 0.1 eV and consequently the increase in Schottky barrier height on β-Ga_2O_3 by about 0.8 eV compared to the plain Pt.[33–36] The active oxygen plasma during the formation of PtO_x by reactive sputtering could introduce additional oxygen to reduce interfacial oxygen vacancies and passivate the interface, consequently increasing the Schottky barrier height of PtO_x on the surface of oxides.[37,38] In addition, a top Pt layer sputtered on the PtO_x contact layer could work as a capping layer to ensure an equipotential surface,[39] while our group has demonstrated that the sputter deposition of PtO_x/Pt bilayer on β-Ga_2O_3, κ-Ga_2O_3, and a-Ga_2O_3 epitaxial thin films exhibited good performance in Schottky barrier diodes (SBDs).[40–42] Hence, the bilayer PtO_x/Pt Schottky gate contact is made by sputter deposition for fabricating MESFETs in this work.

II. EXPERIMENTAL DETAILS

A. Preparation of PLD targets and deposition of thin films

The homogeneous bulk targets for PLD were fabricated through a two-step sintering process: the pressed pellets of a mixture of GeO_2 (purity 99.999%, ChemPUR) and β-Ga_2O_3 (purity 99.99%, Alfa Aesar) raw powders in various weight ratios (40 wt. % Ga_2O_3 and 60 wt. % GeO_2, 20 wt. % Ga_2O_3 and 80 wt. % GeO_2, 10 wt. % Ga_2O_3 and 90 wt. % GeO_2, 5 wt. % Ga_2O_3 and 95 wt. % GeO_2, 2.5 wt. % Ga_2O_3 and 97.5 wt. % GeO_2) were first sintered at 1050 °C for 12 h in air, the resulting pellet was crushed and ground into fine powders for the sintering at 1090 °C for 12 h in air to obtain the PLD targets. The Ga:Ge atomic ratio of the target made of 5 wt. % Ga_2O_3 and 95 wt. % GeO_2 raw powders is calculated to be approximately 1:17. A 248 nm KrF excimer laser (Coherent LPX Pro 305) with a 5 Hz repetition was used for PLD with a laser fluence of about 3.5 J/cm^2 on the target surface.

B. Microstructural characterizations

A PANalytical X'Pert PRO MRD high-resolution x-ray diffraction (XRD) system with hybrid 2-bounce Ge (220) monochromator (Cu $K\alpha_1$, $\lambda = 1.5406$ Å) was used to perform the out-of-plane and tilted-angle 2theta-omega scans, skew-symmetric phi-scan, rocking curves, and asymmetric reciprocal space mapping (RSM) for investigating the microstructure of films. The film thickness was calibrated using x-ray reflectometry without the monochromator.

The Ga and Ge atomic contents in films deposited by using the five different Ge-rich targets made of different Ga_2O_3 vs GeO_2 weight ratios were determined by scanning electron microscopy (SEM) with energy-dispersive x-ray spectroscopy (EDS) using an FEI Nova 200 NanoLab microscope equipped with a Bruker Quantax 200 EDS detector. The K-series signals of EDS spectra were used while the average value of three results measured on three different areas of each film surface was taken.

A Park System XE-150 atomic force microscopy (AFM) was used to study the surface morphology of films.

The cross-sectional microstructures of an epitaxial thin film layer were investigated by transmission electron microscopy (TEM)

operating at 300 kV and the scanning transmission electron microscopy with energy-dispersive x-ray spectroscopy (STEM-EDS) using a FEI TITAN3 G2 80-300 microscope equipped with a Thermo Fisher FEI Super-X EDS detector. The cross-sectional TEM lamella was prepared by focused ion beam (FIB) machining employing a Zeiss Crossbeam-Auriga 40 FIB-SEM equipped with a gas injection system (Pt, C). Before the site-specific lift-out, the film surface was protected with a thin carbon bar, which was deposited with the help of the electron beam before the actual platinum protection bar was deposited by cracking the precursor gas with the ion beam. After uncovering the lamella, it was transferred *in situ* with a needle manipulator to a Cu grid and thinned to electron transparency.

Depth profiling of thin film by the time-of-flight secondary ion mass spectrometry (TOF-SIMS) was carried out using a TOF-SIMS M6 instrument (IONTOF GmbH, Germany). A primary ion source of Bi-cluster LMIS was used for TOF-SIMS analysis. The depth profiling in negative polarity was performed by using a sputter gun of Cs ion beam for ion etching and a flood gun of low energy electrons for charge compensation. The area sizes are $300 \times 300\,\mu m^2$ and $100 \times 100\,\mu m^2$ for sputtering and analysis, respectively.

A Thermo Scientific Nexsa G2 x-ray photoelectron spectrometer with a hemispherical analyzer was used for x-ray photoelectron spectroscopy (XPS) analysis. The survey spectra, core-level spectra, and valence band spectra of the sample were acquired using a monochromatic Al Kα x-ray source (E = 1486.6 eV) and a flood gun of low energy electrons for charge compensation. Survey spectra were acquired with a 1 eV step size, a 200 eV pass energy, and the 100 ms dwell time. High-resolution XPS (HR-XPS) core-level spectra and valence band spectra were acquired with a 0.1 eV step size, a 40 eV pass energy, and the 500 ms dwell time. Binding energy shifts due to the surface charging effect were corrected by using the C 1s level of adventitious carbon at 284.8 eV as a reference. The Shirley background was used for data fitting.[43]

All the above measurements were performed at room temperature.

C. Device fabrication of SBDs and MESFET

The two lateral Schottky barrier diodes (SBDs) were fabricated through sputter deposition of PtO_x/Pt(28 nm) bilayer Schottky contacts (SCs) on the surface-etched γ-$(Ga_{0.8}Ge_{0.2})_2O_3$ epitaxial thin films after the surface pretreatment by 45 s Ar/O_2 plasma etching and 30 s Ar plasma etching, respectively, using a PlasmaPro NGP80 ICP system (Oxford Instruments). The 45 s Ar/O_2 plasma etching treatment (25/25 SCCM Ar/O_2, $p = 20$ mTorr, HF = 250 W, ICP = 300 W) could etch to a depth of about 4 nm, while the 30 s Ar plasma etching (50 SCCM Ar, $p = 20$ mTorr, HF = 250 W, ICP = 300 W) could etch to a depth of about 3 nm. The SCs were structured into circular contacts by photolithography. SCs were deposited by reactive DC sputtering of Pt in pure O_2 (100 SCCM) and subsequently mixed with Ar/O_2 (50/50 SCCM) using a 30 W sputtering power. Afterward, a metallic Pt capping layer was *in situ* sputtered in inert Ar (100 SCCM) atmosphere at the same sputtering power, and this Pt layer works as capping to ensure an equipotential surface.[39] In the second process of Ohmic contact formation, plasma etching treatment with 50 SCCM Ar for 30 s was performed on the region of Ohmic contact layer stacks defined by photolithography to reduce the contact resistance. Mo(30 nm)/Au (100 nm) bilayer was deposited in pure Ar atmosphere by DC sputtering and the final step of lift-off was carried out.

In the first step of MESFET device fabrication, the surface pretreatment by Ar/O_2 plasma etching was performed for 45 s (etched depth of about 4 nm). For Ohmic contact formation, the source and drain patterns of ring-gate FET were made by a photolithography process, followed by Ar plasma etching for 30 s. Then Ohmic contacts were fabricated by sputter deposition of Mo(30 nm)/Au (100 nm) bilayer and lift-off. After the ring-gate patterning achieved by a photolithography process, Schottky gate was finally formed by sputter deposition of PtO_x/Pt (28 nm) and lift-off.

D. Measurements on electrical properties

A Physical Property Measurement System (PPMS, Quantum Design) was used to perform the temperature-dependent Hall effect measurements at a 6 T magnetic field by using the four-electrode van der Pauw method. The current–voltage (I–V) measurements were carried out in a Süss Waferprober system P200 using an Agilent 4155C Semiconductor Parameter Analyzer at room temperature.

III. RESULTS AND DISCUSSION

Figure 1(a) shows XRD 2θ-ω scans of the films deposited with 18 000 pulses (5 Hz repetition) under 0.0005 mbar oxygen partial pressure at different temperatures. The 2θ-ω scans were calibrated according to the $MgAl_2O_4$ (004) reflex at 44.830° ($a = 8.08$ Å). There is no apparent crystalline film obtained at 600 °C. The film thickness is determined to be about 154 and 180 nm for the thin film grown at 650 and 680 °C, respectively, by x-ray reflectivity (XRR).[44,45] From the rocking curves of (004) peaks shown in Fig. 1(b), the optimal deposition temperature is 650 °C to grow a high-quality (001)-oriented γ-$(Ga_{1-x}Ge_x)_2O_3$ (GGO) film with a full width at half maximum (FWHM) of the rocking curve of (004) peak of about 0.03°. Figure 1(c) exhibits the tilted-angle XRD pattern of (111) $MgAl_2O_4$ plane, revealing the orientation relationship of [111] GGO//[111] $MgAl_2O_4$. The phi scan results shown in Fig. 1(d) demonstrate that the four peaks of (226) reflection of (001) GGO film are placed on those of (001) $MgAl_2O_4$ substrates, revealing the in-plane epitaxial relationships of [010] GGO//[010] $MgAl_2O_4$ and [110] GGO//[110] $MgAl_2O_4$, and indicating a cube-on-cube epitaxy. The (004) reflection peak of 154 nm thick epitaxial film deposited at 650 °C located at about 43.628°, indicating an out-of-plane lattice constant of about 8.29 Å that is close to the reported γ-Ga_2O_3 lattice constant of 8.24 Å.

In addition, the influences of oxygen partial pressures and targets' compositions on the film samples deposited at 650 °C were investigated by XRD and SEM-EDS analysis, see the results in Figs. S1 and S2 and Table S1 of the supplementary material, and it is suggested that the optimal oxygen pressure is 0.0005 mbar while the suitable target is made of 5 wt. % β-Ga_2O_3 and 95 wt. % GeO_2 for growing the high-quality epitaxial thin films with the evaluated cationic content of Ga and Ge by SEM-EDS of about

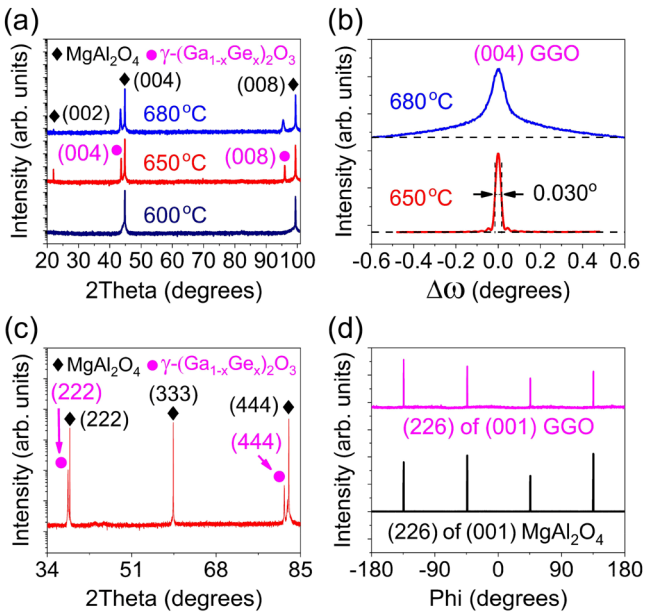

FIG. 1. (a) XRD 2θ-ω scans and (b) rocking curves of (004) reflexes of thin films deposited at the indicated temperatures. (c) Tilted-angle XRD pattern of (111) $MgAl_2O_4$ plane of the film sample deposited at 650 °C. (d) Phi scans of (226) reflections for the (001)-oriented thin film deposited at 650 °C and the (001) $MgAl_2O_4$ substrate, respectively.

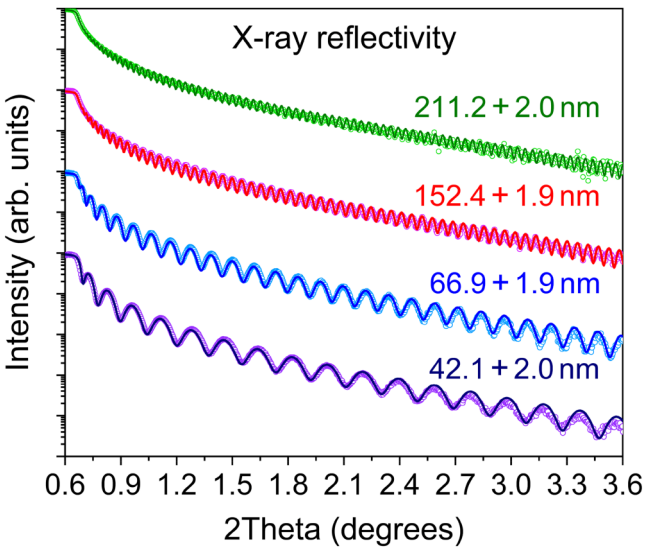

FIG. 2. Simulation (solid lines) and experiment (hollow circles) of x-ray reflectivity (XRR) of epitaxial thin films with different in-total thicknesses of about 44, 69, 154, and 213 nm, estimated by XRR.

78.9 ± 6.4 at. % and 21.1 ± 1.7 at. %, respectively. The (001)-oriented epitaxial thin films would be nominal γ-$(Ga_{0.8}Ge_{0.2})_2O_3$ alloy thin films.

To study the thickness-dependent microstructural properties, we grew the epitaxial (001) γ-$(Ga_{0.8}Ge_{0.2})_2O_3$ thin films with various thicknesses in a range of around 40–210 nm under 0.0005 mbar oxygen partial pressure at 650 °C. Figure 2 presents the experimental XRR patterns (hollow circles) of four film samples, exhibiting clear XRR fringes (Kiessig fringes). The thickness of the four films is determined to be about 44, 69, 154, and 213 nm, respectively, according to the position and spacing of intensity minima of XRR fringes without a model fitting.[44,45] The experimental XRR data of films are used to further investigate the film surface structure by the model fitting using a GenX 3 software.[46] The single layer model could not give a reasonable fit result; thus, a two-layer stack model composed of a main film layer and a top surface layer is used to construct the film structure and achieve good simulation results, which show a good fit to the experimental XRR results, as depicted in Fig. 2. The simulation parameters are shown in Table S2 of the supplementary material. It is suggested that there exists a relatively denser surface layer with a thickness of about 2 nm covering the epitaxial film layers, whose thickness is evaluated to be about 42.1, 66.9, 152.4, and 211.2 nm, respectively.

Figure 3(a) presents the selected (004) peaks of epitaxial films exhibiting clear Laue interference fringes, which were simulated by using the Laue interference function to evaluate the thickness of high-quality epitaxial film layers of about 42.3, 67.2, 152.6, and 211.3 nm as labeled, respectively. The (004) peaks are around 43.628° for the 42.3–152.6 nm thick epitaxial layers while the 211.3 nm thick epitaxial layer shows a slightly right-shift (004) peak at 43.650° (probably a slight deviation in composition resulting from the non-uniformity of Ge-rich target), representing the out-of-plane lattice constant c of about 8.29 Å, which is a little bit greater than the bulk γ-Ga_2O_3 lattice constant value of 8.24 Å. Considering the variable integral number (N) of coherently diffracting unit cells with a lattice constant (c) of about 8.29 Å in the out-of-plane direction, the expression of Laue interference function (scattered intensity I as a function of angle θ) is given by[45,47]

$$I(\theta) \propto [\sin(2\pi Nc \sin\theta/\lambda)/\sin(2\pi c \sin\theta/\lambda)]^2, \quad (1)$$

where λ (1.5406 Å) is the wavelength of Cu Ka_1 x-ray source.

The pristine 213 nm thick film (with the 211.3 nm thick epitaxial film layer) was etched by Ar plasma to be the thinner film layers with a thickness of about 167.4 and 116.9 nm, respectively, estimated by the simulation of Laue interference fringes, for investigating the film layer thickness-dependent FWHM of rocking curves. From Fig. 3(b), there is no apparent peak shift observed for the film layers before and after the Ar plasma etching treatments. The simulation and experimental results of Laue interference fringes of total 44 and 213 nm thick pristine epitaxial films with the evaluated film layer thickness of about 42.3 and 211.3 nm are shown as a representative illustration in Figs. 3(c) and 3(d), respectively. The simulation results of Laue interference fringes around the (004) reflections of 67.2, 116.9, 152.6, and 167.4 nm thick epitaxial film layers are shown in Fig. S4 of the supplementary material. The remarkably good agreement between the simulation

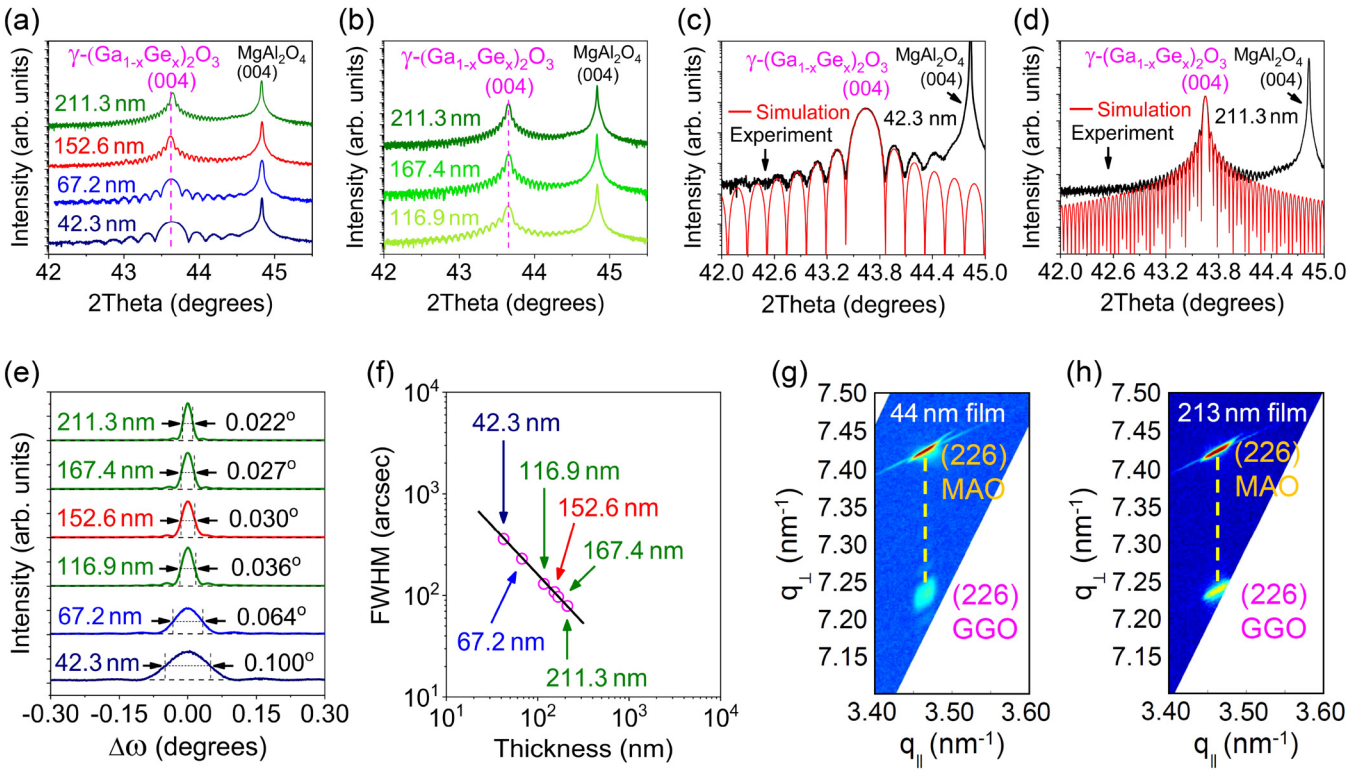

FIG. 3. Selected (004) peaks of XRD patterns of (a) the four samples of high-quality epitaxial films and (b) the pristine 213 nm thick film before and after Ar plasma etching treatments with the indicated thicknesses of epitaxial film layers evaluated by simulation of Laue interference fringes around (004) reflections. (c) and (d) Simulation results (red plots) of Laue interference fringes around the (004) reflections of epitaxial thin films with the indicated film layer thicknesses estimated by simulation using the Laue interference function. (e) Rocking curves of (004) reflexes, and (f) double logarithmic plot of the rocking curve FWHM vs the film layer thickness for epitaxial film layers with the thicknesses as labeled. (g) and (h) Reciprocal space mapping of (226) diffraction spots of the 44 nm (~42.3 nm epitaxial layer) and 213 nm (~211.3 nm epitaxial layer) thick pristine (001) γ-$(Ga_{0.8}Ge_{0.2})_2O_3$ (GGO) films and the (001) $MgAl_2O_4$ (MAO) substrates.

and experiment is obtained considering that the Laue fringes arise from the out-of-plane stacking of 51 unit cells ($c = 8.290$ Å), 81 unit cells ($c = 8.292$ Å), 141 unit cells ($c = 8.289$ Å), 184 unit cells ($c = 8.293$ Å), 202 unit cells ($c = 8.287$ Å), and 255 unit cells ($c = 8.288$ Å), respectively, which result in the total thickness of about 42.3, 67.2, 116.9, 152.6, 167.4, and 211.3 nm for the epitaxial film layers. Those thickness values are very close to the above results evaluated by XRR model fittings.

Figure 3(e) shows the rocking curves of (004) reflections of the film layers with various thicknesses. The value of FWHM of rocking curves decreases from 0.100° to 0.022° as the thickness of epitaxial film layers increases from 42.3 to 211.3 nm. In the double logarithmic plot of FWHM vs thickness shown in Fig. 3(f), a nearly inverse linear relationship is observed,[48] suggesting that the broadening rocking curve for the thinner epitaxial (001) γ-$(Ga_{0.8}Ge_{0.2})_2O_3$ films probably results from the large number of crystal defects formed at the initial growth stage of epitaxial thin

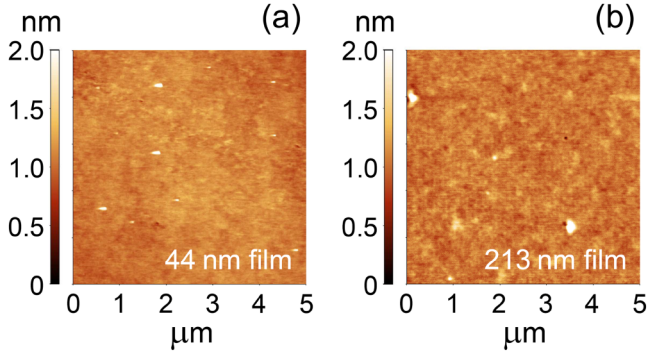

FIG. 4. AFM surface morphologies of pristine thin films (composed of top surface layer and epitaxial film layer) with the evaluated in-total thickness of about (a) 44 and (b) 213 nm, respectively.

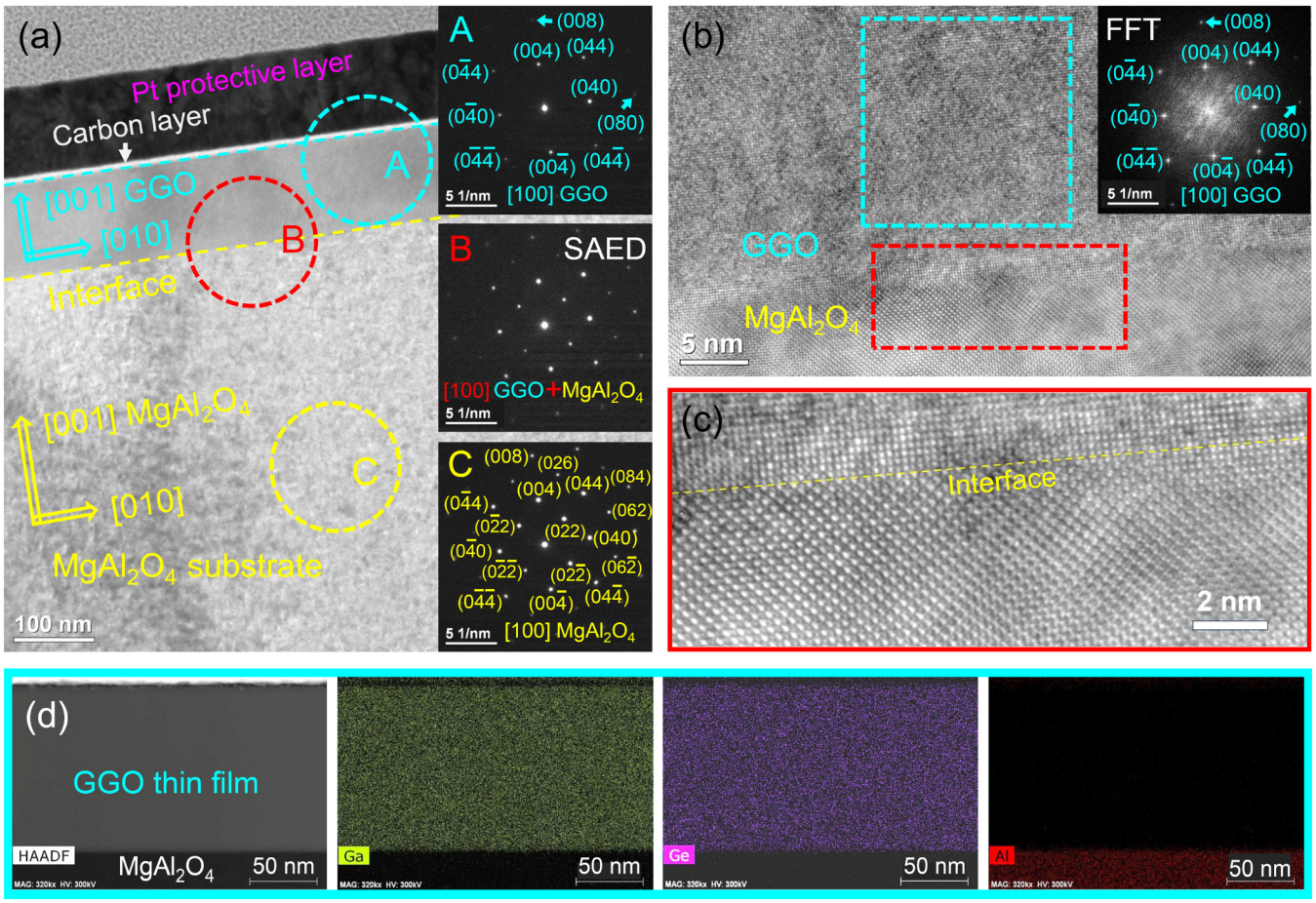

FIG. 5. (a) Cross-sectional TEM brightfield image with inserted SAED patterns of a 116.9 nm thick film sample. (b) High-resolution image of interface with an inset of FFT patterns for the selected film region. (c) High-resolution atomic lattice image for the selected interface region (with red dot line frame) on image (b). (d) HAADF-STEM image and EDS mappings of Ga, Ge, and Al elements.

films, while defect's concentration significantly decreases as the high-quality epitaxial thin films grow with increasing thickness. A similar scenario was found previously in the lattice-match heterostructure of high-quality GaInAs alloy layers grown on (001) GaAs single crystal substrates.[48] Figures 3(g) and 3(h) present the reciprocal space mapping of (226) diffraction spots of the 44 and 213 nm thick pristine films, and the substrates. It is obvious that the films and substrates have nearly the same in-plane reciprocal coordinates, indicating their similar in-plane lattice constants of about 8.08 Å, which is a little smaller than the out-of-plane lattice constant of films of about 8.29 Å (tetragonality of 1.026). In the in-plane direction, the narrow (226) diffraction spots demonstrate that the films are constrained by the substrates throughout the films, and epitaxial films are almost fully strained.

The introduction of Ge into γ-Ga_2O_3 through alloying reduces the unit cell volume while increasing the molar mass due to the smaller ionic radius of Ge^{4+} and the larger atomic mass of Ge and subsequently increases the density of alloy thin films. The calculated density of nominal γ-$(Ga_{0.8}Ge_{0.2})_2O_3$ epitaxial thin film layers is about 6.17 g/cm^3, which is larger than the experimentally evaluated density of γ-$(Ga_{0.8}Ge_{0.2})_2O_3$ epitaxial thin film layers of about 5.92 g/cm^3 through the model fitting of XRR data as shown in Table S2 of the supplementary material. Similarly, the calculated density of γ-Ga_2O_3 is about 5.94 g/cm^3 whereas the experimentally measured density of γ-Ga_2O_3 is about 5.76 g/cm^3.[3] The hypothesis on change in density of γ-Ga_2O_3-based alloy thin films after alloying with Ge agrees well with the calculated and experimental results in this study. In addition, the out-of-plane lattice expansion of fully strained alloy thin films, leading to a little bit greater lattice constant of about 8.29 Å compared to γ-Ga_2O_3 lattice constant of 8.24 Å, is apparently due to the in-plane compressive strain of the alloy films. Also, the presence of Ge^{2+} cations, revealed by XPS later, is likely to increase the out-of-plane lattice constant due to a general increase in the lattice constant because the ionic radius of

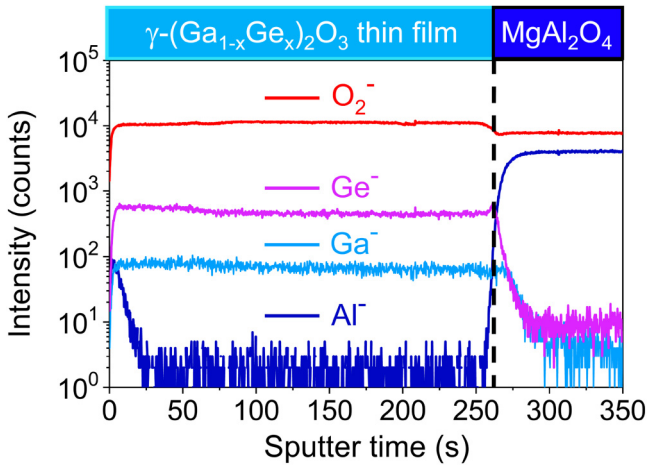

FIG. 6. TOF-SIMS depth profile of the pristine 154 nm thick epitaxial (001) γ-$(Ga_{0.8}Ge_{0.2})_2O_3$ film grown on (001) $MgAl_2O_4$ substrates.

Ge^{2+} preferably occupying the octahedral site is 0.73 Å and greater than that of Ga^{3+} cations.[28]

AFM surface morphologies shown in Fig. 4 demonstrate a smooth surface of the 44 and 213 nm thick pristine films with the RMS roughness of about 0.23 and 0.14 nm, respectively. Combining with the AFM images of the 154 nm thick pristine film shown in Fig. S3 of the supplementary material, it is noteworthy that the high-quality epitaxial (001) γ-$(Ga_{0.8}Ge_{0.2})_2O_3$ pristine films do not show any apparent crystalline grains and clear grain boundaries.

The 116.9 nm thick γ-$(Ga_{0.8}Ge_{0.2})_2O_3$ (GGO) epitaxial film (original 213 nm thick film) after Ar plasma etching was further investigated by TEM. The cross-sectional brightfield image shown in Fig. 5(a), combined with the images with various magnifications shown in Fig. S5 of the supplementary material, indicates a single crystal film structure without any crystalline grains and grain boundaries observed, which is consistent with the above AFM observation. The three insets in Fig. 5(a) display selected area electron diffraction (SAED) patterns corresponding to marked A (epitaxial film layer), B (interface), and C (substrate) areas, confirming the in-plane orientation relationships of [010] GGO//[010] $MgAl_2O_4$ and [110] GGO//[110] $MgAl_2O_4$. Figure 5(b) exhibits a very sharp interface without any transition layers and impurity phases. Figure 5(c) presents a high-resolution image of an atomic lattice matched coherent interface. The evaluated cationic content of Ga and Ge by STEM-EDS is about 78.5 ± 2.4% and 21.5 ± 0.6%, respectively, see the analysis result in Fig. S6 of the supplementary material. The nominal composition of epitaxial alloy thin films is further verified to be γ-$(Ga_{0.8}Ge_{0.2})_2O_3$ with an inverse disordered spinel structure. The introduced Ge cations should randomly distribute at both octahedral and tetrahedral sites of the defective inverse disordered spinel structure γ-Ga_2O_3, which could be attributed to the probably preferential occupation of vacant cation sites as well as the substitution of Ga^{3+} cations that randomly occupy octahedral and tetrahedral sites in the γ-Ga_2O_3.[7] It is noteworthy that the diffraction spots belonging to {022} and {026} plane families unexpectedly vanished into the SAED pattern of epitaxial layer, which probably resulted from the likely short-range disorder of sublattices caused by introducing high-concentration Ge cations into the γ-Ga_2O_3 crystal lattice.[49] The formation of single crystal structure of heteroepitaxial binary alloy oxide thin films grown by PLD probably corelates to the intrinsic feature of high lattice distortion tolerance of the defective disordered inverse spinel γ-Ga_2O_3 structure.[7,16,49] The EDS mappings of Ga and Ge elements shown in Fig. 5(d) indicate the uniform elemental distribution over the entire film thickness. Figure 6 shows the TOF-SIMS depth profiling of 154 nm thick pristine films, also confirming the uniform chemical composition throughout the film.

Figure 7(a) shows the XPS survey spectra of the pristine film surface and Ar plasma sputtered (etched depth is about 10 nm) surface of a pristine ~210 nm thick epitaxial film, indicating that no additional impurity elements are detected. The selected Ge 2*p* and Ga 2*p* peaks of XPS survey spectra are presented in Fig. 7(b). The 2*p* electrons with the relatively low kinetic energy have a shallower sampling depth and a better surface sensitivity compared to the high kinetic energy 3*d* electrons. It is apparently observed that the pristine film surface shows much more Ge content than that of the Ar-plasma sputtered film surface. It is suggested that the pristine surfaces of epitaxial (001) γ-$(Ga_{0.8}Ge_{0.2})_2O_3$ alloy thin films are covered by a thin Ge-rich top surface layer, which corresponds to the about 2 nm thick surface layer estimated by the XRR model fitting. This Ge-rich surface layer probably results from the surface segregation of Ge as well as the surface adsorption of gas-phase GeO_x plasmas by laser evaporation of the Ge-rich target surface.

The composition and chemical states of Ga and Ge of the pristine 154 nm thick epitaxial film were analyzed by high-resolution XPS after the surface cleaning by Ar plasma etching to a depth of about 20 nm. It is normally believed that, compared to 2*p* electrons with low kinetic energy, the relatively high kinetic energy 3*d* electrons have a deeper sampling depth. Figure 7(c) demonstrates the valence band spectrum together with the core-level spectra of Ga 3*d* and Ge 3*d* whose spin–orbit splitting (into $3d_{3/2}$ and $3d_{5/2}$) has been ignored for curve fittings due to their relatively small splitting (peak separation) of only about 0.46 and 0.58 eV, respectively. The valence band maximum (VBM) is determined to be about 3.3 ± 0.1 eV below the Fermi level. The relative sensitivity factor (areal factor for the system setup) of Ga 3*d* and Ge 3*d* is 1.412 and 1.294, respectively, for calculating the cationic concentration of Ga and Ge in the thin film. The Ga 3*d* peak shows two components of Ga^{3+} (90.5 at. %) and Ga^{1+} (9.5 at. %) in oxide states with an FWHM of 1.49 eV centering at 20.5 and 19.1 eV, respectively.[50–53] While Ge 3*d* core-level spectrum exhibits two oxide states of Ge^{2+} (13.0 at. %) and Ge^{4+} (87.0 at. %) with an FWHM of 1.58 eV centering at 31.0 and 32.5 eV, respectively.[31,54,55] The calculated cationic content of Ga and Ge is about 78.4% and 21.6%, respectively, which are consistent with the analysis result by STEM-EDS. According to the energy loss feature of O 1*s* core-level spectrum exhibited in the inset of Fig. 7(d), the direct bandgap is determined to be about 5.2 ± 0.1 eV, which is very close to the direct optical bandgap of 5.17 eV evaluated by Tauc plot from transmission spectrum shown in Fig. S7 of the supplementary material.

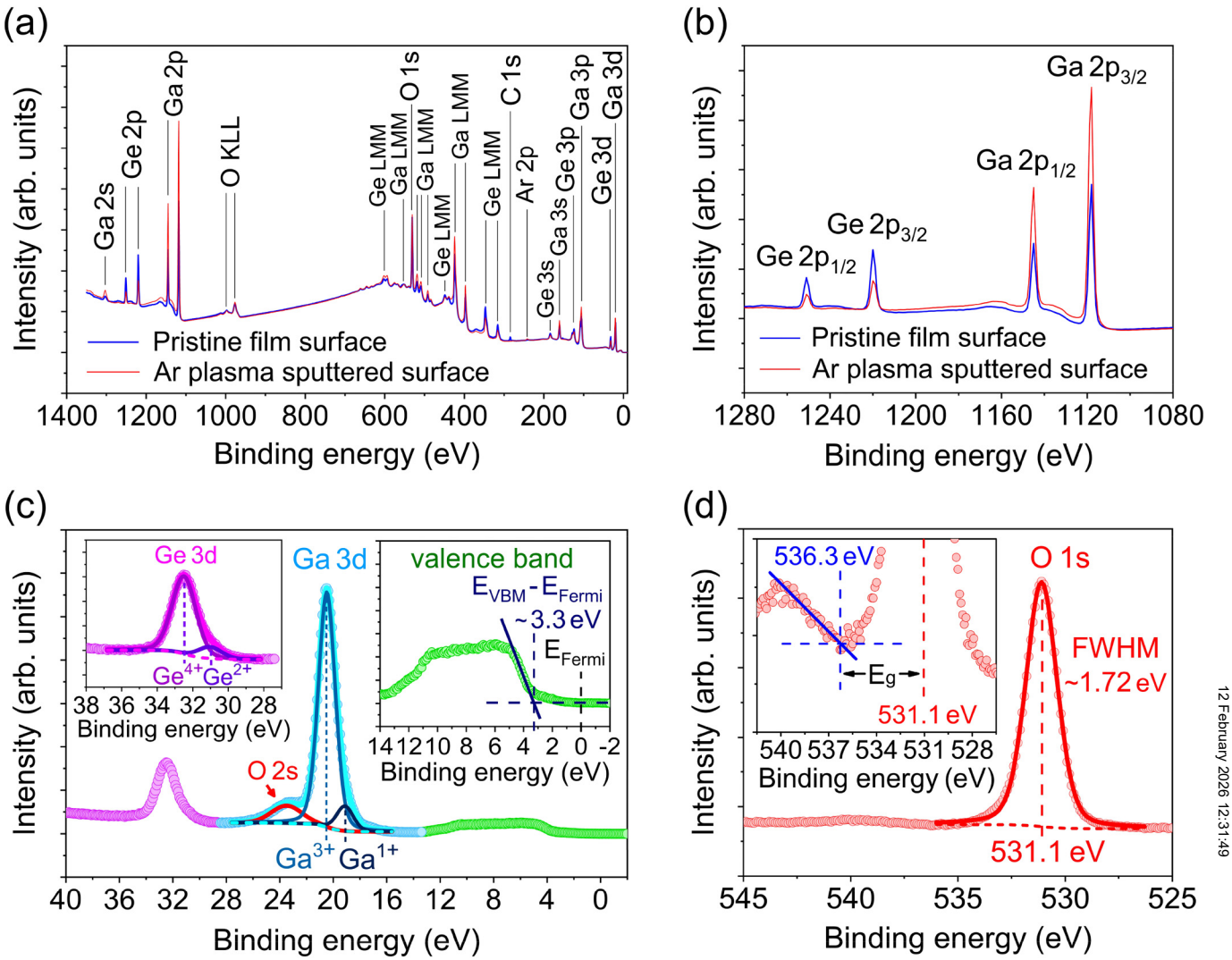

FIG. 7. (a) XPS survey spectra of the pristine film surface and the Ar plasma sputtered (etching to a depth of about 10 nm) surface of a pristine ~210 nm thick epitaxial film and (b) the selected Ge 2*p* and Ga 2*p* peaks. HR-XPS core-level spectra with fittings of (c) Ga 3*d* and Ge 3*d* components together with the valence band spectrum as an inset and (d) O 1s component with inserted energy loss feature of the pristine 154 nm thick film after surface cleaning by Ar plasma etching.

In contrast to only the noise signal (too small current over the range of current meter) observed in current–voltage (I–V) test on the top surface of pristine thin films, an almost Ohmic behavior is observed for the films etched by Ar plasma for 30 s (about 3 nm etched depth) in the two-terminal I–V characteristic shown in Fig. 8(a). The highly insulating top surface of pristine films probably correlates to about 2 nm Ge-rich oxide surface layer, which also likely results in a great contact resistance with Mo/Au electrodes.[32] Normally surface treatment of oxides by Ar plasma etching could induce large-density surface defects including oxygen vacancies that enhance surface conductivity and reduce contact resistance, causing a better Ohmic contact. For temperature-dependent Hall effect measurements, Mo(30 nm)/Au(150 nm) electrodes were deposited on the etched surface of films for the four-electrode van der Pauw method. Figure 8(b) presents a typical semiconductor behavior with a dramatic decrease in resistivity with increasing temperature from 175 to 350 K. The films with different thicknesses show very similar resistivity of around 30 Ω cm at 350 K while a relatively high resistivity of about 10 000 Ω cm below 200 K. From Fig. 8(c), the Hall electron carrier concentration of films increases from about 10^{15} cm^{-3} at 200 K to about 10^{17} cm^{-3} at 350 K with about 180 meV activation energy.[56] The Hall electron carrier mobility, as shown in Fig. 8(d), rises gradually from about 1 to 3 cm^2 V^{-1} s^{-1} as the temperature increases from 200 to 350 K.

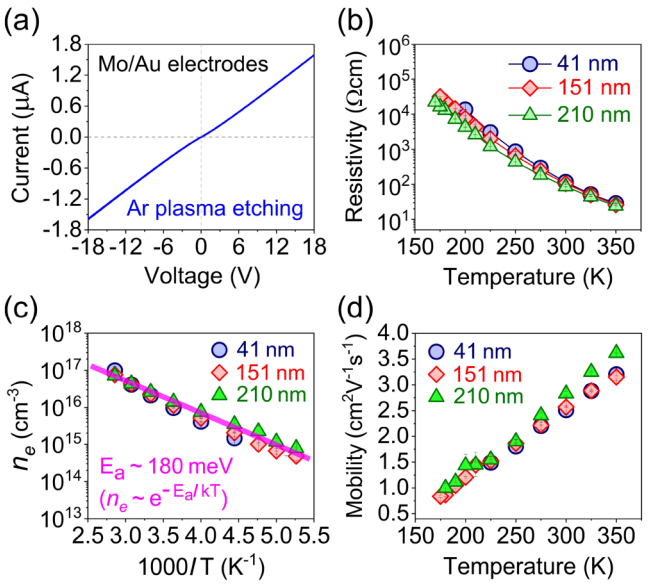

FIG. 8. (a) I–V characteristic measured between two Mo/Au electrodes. Hall effect measurements from 175 to 350 K: (b) resistivity, (c) electron carrier concentrations, and (d) Hall electron carrier mobility of epitaxial films with the indicated thicknesses after Ar plasma etching.

In principle, doping of 1 at. % Ge^{4+} to substitute Ga^{3+} in γ-Ga_2O_3 could contribute a high electron concentration much over 1.0×10^{20} cm^{-3} (nominal Ga atomic density of about 3.8×10^{22} cm^{-3} in a γ-Ga_2O_3 unit cell with a 8.24 Å lattice constant).[3] The presence of Ga^{1+} and Ge^{2+} cations in films to substitute Ga^{3+} could generate holes to neutralize the electrons resulting from the substitution of Ga^{3+} by Ge^{4+}. The calculated concentration of additional electrons is about 1 at. % of cations in γ-$(Ga_{0.8}Ge_{0.2})_2O_3$ alloy thin films, which might supply major electron carriers with a high concentration of more than 10^{20} cm^{-3} that is 1000 times of magnitude higher than the measured Hall electron carrier concentration of about 10^{17} at 350 K, implying that the Ge alloying and self-doping antisite cations in the inverse spinel structure alloy thin films do not provide effective free carriers. Considering that the Ge^{4+} cation is a shallow-level donor dopant in β-Ga_2O_3,[57] it is supposed that the n-type conductivity in γ-$(Ga_{0.8}Ge_{0.2})_2O_3$ alloy thin films results from the minor effective doping of Ge^{4+} to substitute Ga^{3+} in a small number of specific sites, at which the Ge^{4+} dopants could supply free electron carriers. The partially subvalent Ge^{2+} and Ga^{1+} cations co-exist with mainly normal Ge^{4+} and Ga^{3+} cations in the disordered inverse spinel alloy thin films, suggesting the presence of a certain amount of various antisite cationic defects in films, which undoubtedly complicates the ionic state and local charge state as well as the electronic band structure of alloy thin films. The ionized and charged impurities correlated to high-concentration Ge^{4+} as well as subvalent Ge^{2+} and Ga^{1+} cations probably cause serious scattering to remarkably limit the electron mobility in the epitaxial film layers. An understanding of the mechanism of free carrier generation and transport requires further study in the future.

To ensure an effective Schottky gate contact for the MESFETs based on (001) γ-$(Ga_{0.8}Ge_{0.2})_2O_3$ epitaxial thin films, the influence of surface pretreatment by the Ar plasma etching and Ar/O_2 plasma etching on the Schottky contacts in SBDs based on the epitaxial films was first investigated. The 45 s Ar/O_2 plasma etching and 30 s Ar plasma etching could etch to a depth of about 4 and 3 nm, respectively. See the thickness evaluation by XRR model fittings for epitaxial films before and after the plasma etching treatments in Fig. S9 and Table S3 of the supplementary material. Figure 9(a) presents the schematic of SBDs device design and a top-view micrograph of the lateral SBDs based on the pristine 154 nm thick epitaxial films. The SBD devices were fabricated through sputter deposition of PtO_x/Pt bilayer Schottky contacts on the etched surface of films after the first step of plasma etching surface pretreatment. From Fig. 9(b), the SBDs were realized after a 45 s Ar/O_2 plasma etching pretreatment. The surface treatment by O_2 plasma etching normally could substantially reduce the amount of oxygen vacancies on the oxide thin film surface,[58] and hence remarkably improve the Schottky contacts on oxide thin films.[59] In the case of this study, the 45 s Ar/O_2 plasma etching pretreatment could not only remove the 2 nm thick insulating Ge-rich surface layer of pristine films but also lead to a good PtO_x/Pt Schottky contact on the epitaxial (001) γ-$(Ga_{0.8}Ge_{0.2})_2O_3$ alloy thin films.

As the first demonstration of γ-Ga_2O_3 film-based FETs, we used the pristine 44 nm thick γ-$(Ga_{0.8}Ge_{0.2})_2O_3$ film (about 40 nm thickness after the surface pretreatment by 45 s Ar/O_2 plasma etching) as n-type channel layer to fabricate the MESFETs. The thinner channel layer is normally easier to form the fully depleted channel layer on insulator substrates to reduce the off-state leakage of devices. A circular ring-gate FET pattern was employed for the device demonstration due to a lack of device isolation technique. The cross-sectional schematic of MESFET device design and top-view micrograph of the fabricated MESFET device are shown in Fig. 9(c). The lateral circular MESFET device with a diameter of the ring-gate electrode of 750 μm has a 10 μm gate length (L_G) and a 40 μm source-drain spacing (L_{SD}). Figure 9(d) presents DC output characteristics, indicating a typical gate-modulated I–V characteristic with a maximum drain current (I_{DS}) of about 140 nA at $V_{GS} = 2$ V. Figure 9(e) demonstrates the logarithmic plots of transfer curves at different V_{DS} from 5 to 12.5 V, together with the linear plot of square root I_{DS} vs V_{GS} at $V_{DS} = 12.5$ V, apparently presenting a linear relationship region of I_{DS} vs V_{GS} for $V_{GS} < 2$ V, which is an ideal feature of MESFETs. The clockwise hysteresis of transfer curves probably arises from electron trap states at the interface between the Schottky gate contact and the n-type channel layer. All of the transfer curves exhibit a complete pinch-off characteristic for $V_{GS} < -4$ V and an about 10^5 on/off ratio of drain current with a small off-state drain leakage current of about 3 pA. Figure 9(f) shows the three-terminal gate leakage current at $V_{DS} = 12.5$ V and the reverse off-state gate leakage current is about 6 pA which is double the drain leakage current, demonstrating a very small leakage current of the device. All these characteristics suggest a great potential for MESFETs based on inverse spinel γ-Ga_2O_3 semiconductor epitaxial thin films for future

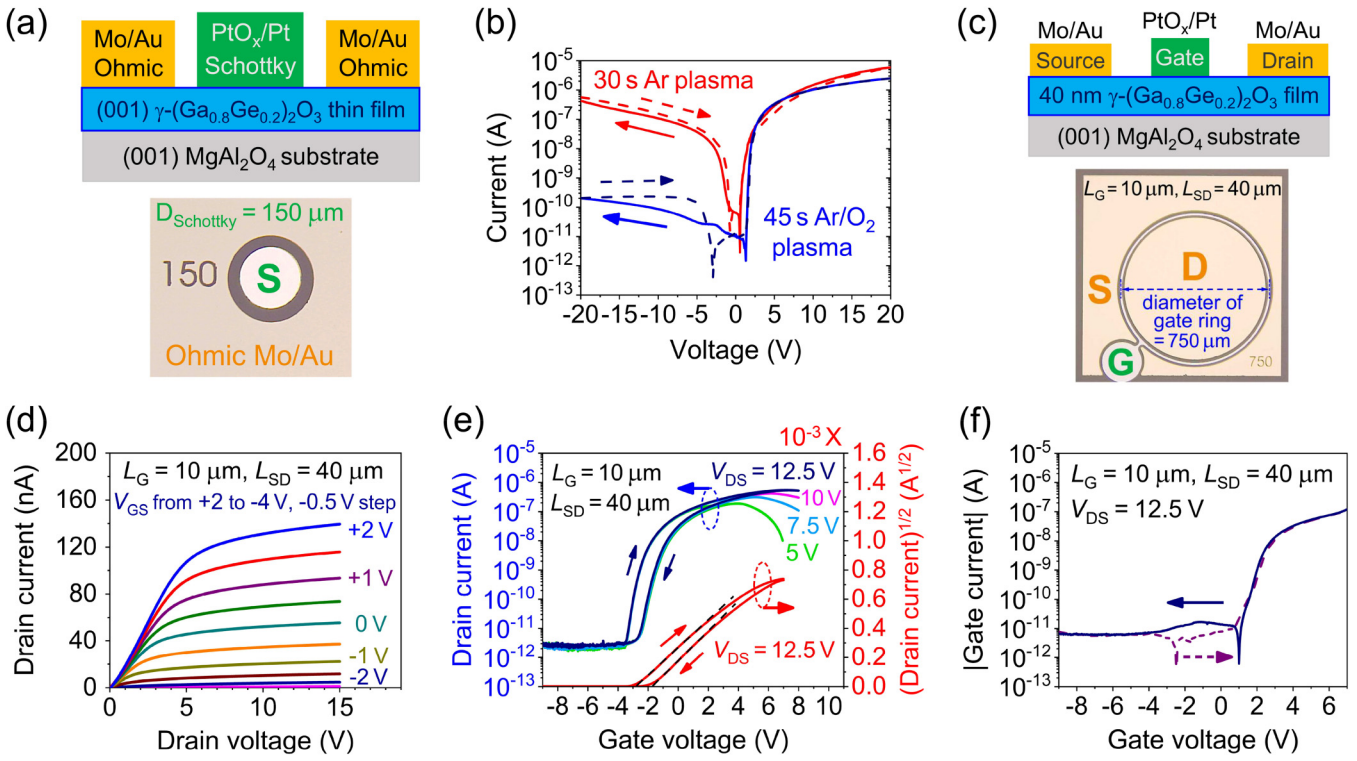

FIG. 9. (a) Cross-sectional schematic of SBDs design (top) and top-view micrograph of the fabricated SBDs (bottom). (b) Double sweep I–V curves of SBDs fabricated after the surface treatment by Ar plasma etching for 30 s and Ar/O_2 plasma etching for 45 s, respectively. (c) Cross-sectional schematic of MESFET device design (top) and top-view micrograph of the fabricated device (bottom), (d) DC output characteristics, (e) transfer characteristics at various V_{DS} as labeled and the square root of I_{DS} vs V_{GS} curve at $V_{DS} = 12.5$ V, and (f) three-terminal gate leakage current of lateral ring-gate MESFET based on the 40 nm film layer after Ar/O_2 plasma etching.

microelectronic device applications, especially in high irradiation environments.[16,49]

IV. CONCLUSIONS

In summary, we demonstrated the epitaxial growth of (001)-oriented γ-$(Ga_{0.8}Ge_{0.2})_2O_3$ alloy semiconductor single crystal thin films with a coherent interface on cubic (001) $MgAl_2O_4$ substrates by PLD. Combining the model fitting of XRR patterns with the simulation of Laue interference fringes to study the thin film structure, together with the electrical properties and XPS surface analysis, it is found that the pristine epitaxial thin films are composed of about 2 nm thick insulating Ge-rich surface layers and high-quality epitaxial n-type semiconductor film layers consisting of partially subvalent Ge^{2+} and Ga^{1+} cations as well as mainly normal Ge^{4+} and Ga^{3+} cations. The direct bandgap of films was determined to be about 5.2 ± 0.1 eV while the valence band maximum was evaluated to be about 3.3 ± 0.1 eV below the Fermi level at room temperature. The temperature-dependent Hall effect measurements indicate that the n-type semiconductor epitaxial thin films have the electron carrier concentration increasing from about 10^{15} cm^{-3} at 200 K to about 10^{17} cm^{-3} at 350 K with an estimated activation energy of about 180 meV. The Hall electron carrier mobility of films rises gradually from about 1 to 3 $cm^2 V^{-1} s^{-1}$ with increasing temperature from 200 to 350 K. We further report a demonstration of epitaxial (001) γ-$(Ga_{0.8}Ge_{0.2})_2O_3$ thin film-based MESFET, which was fabricated through the sputter deposition of PtO_x/Pt bilayer Schottky gate contact realized after the surface pretreatment by 45 s Ar/O_2 plasma etching to a depth of about 4 nm. The MESFET exhibits good DC device characteristics, such as a clear field-effect with the gate voltage-modulated drain current of about 10^5 orders of magnitude for a gate voltage (V_{GS}) swing of -4 to 2 V, a perfect drain current pinch-off for $V_{GS} < -4$ V, and a small gate leakage current of about 6 pA. Our findings offer new insights into microstructural characteristics of ultrawide bandgap inverse spinel oxide semiconductors. This work is also paving the way to the fundamental and application-oriented research on ultrawide bandgap inverse spinel γ-Ga_2O_3-based semiconductor epitaxial thin films as a good candidate of UV transparent conducting oxides and radiation tolerant semiconductors for practical device applications under high irradiation environmental conditions.

SUPPLEMENTARY MATERIAL

See the supplementary material for additional XRD and SEM-EDS analysis results and AFM images, XRR model fitting parameters, TEM images and STEM-EDS spectrum, and UV-vis transmission spectrum.

ACKNOWLEDGMENTS

The authors gratefully thank Monika Hahn at Universität Leipzig for the preparation of PLD targets. Financial support from Deutsche Forschungsgemeinschaft (Grant No. 459722738) is gratefully acknowledged.

AUTHOR DECLARATIONS

Conflict of Interest

The authors have no conflict to disclose.

Author Contributions

Jingjing Yu: Conceptualization (equal); Data curation (lead); Formal analysis (lead); Funding acquisition (supporting); Investigation (lead); Methodology (equal); Software (lead); Validation (equal); Visualization (equal); Writing – original draft (lead); Writing – review & editing (equal). **Sijun Luo:** Conceptualization (lead); Data curation (equal); Formal analysis (equal); Funding acquisition (supporting); Investigation (lead); Methodology (lead); Project administration (lead); Resources (equal); Software (supporting); Supervision (lead); Validation (lead); Visualization (lead); Writing – original draft (equal); Writing – review & editing (lead). **Daniel Splith:** Formal analysis (supporting); Investigation (supporting); Methodology (equal); Resources (equal); Software (supporting); Validation (equal); Writing – original draft (supporting). **Susanne Selle:** Data curation (supporting); Formal analysis (supporting); Funding acquisition (supporting); Investigation (equal); Methodology (equal); Resources (equal); Validation (equal); Visualization (supporting); Writing – original draft (supporting); Writing – review & editing (supporting). **Katrin Thieme:** Investigation (supporting); Methodology (equal); Resources (equal); Validation (supporting); Writing – review & editing (supporting). **Stephan Gierth:** Investigation (supporting); Methodology (supporting); Resources (equal); Validation (supporting); Writing – original draft (supporting). **Thorsten Schultz:** Investigation (supporting); Methodology (supporting); Resources (equal); Validation (supporting); Writing – original draft (supporting). **Peter Schlupp:** Investigation (supporting); Methodology (supporting); Resources (supporting); Writing – review & editing (supporting). **Chris Sturm:** Investigation (supporting); Methodology (supporting); Resources (supporting); Writing – original draft (supporting). **Holger von Wenckstern:** Investigation (supporting); Methodology (supporting); Writing – review & editing (equal). **Michael Lorenz:** Funding acquisition (supporting); Resources (supporting); Writing – review & editing (supporting). **Norbert Koch:** Resources (supporting); Writing – review & editing (supporting). **Thomas Höche:** Resources (supporting); Writing – review & editing (supporting). **Marius Grundmann:** Conceptualization (supporting); Funding acquisition (lead); Resources (lead); Writing – review & editing (supporting).

DATA AVAILABILITY

The data that support the findings of this study are available from the corresponding author upon reasonable request.

REFERENCES

[1]R. Roy, V. G. Hill, and E. F. Osborn, "Polymorphism of Ga_2O_3 and the system Ga_2O_3–H_2O," J. Am. Chem. Soc. **74**, 719–722 (1952).
[2]S. Yoshioka, H. Hayashi, A. Kuwabara, F. Oba, K. Matsunaga, and I. Tanaka, "Structures and energetics of Ga_2O_3 polymorphs," J. Phys.: Condens. Matter **19**, 346211 (2007).
[3]H. Y. Playford, A. C. Hannon, E. R. Barney, and R. I. Walton, "Structures of uncharacterised polymorphs of gallium oxide from total neutron diffraction," Chem. Eur. J. **19**, 2803–2813 (2013).
[4]S. J. Pearton, J. Yang, P. H. Cary IV, F. Ren, J. Kim, M. J. Tadjer, and M. A. Mastro, "A review of Ga_2O_3 materials, processing, and devices," Appl. Phys. Rev. **5**, 011301 (2018).
[5]M. Higashiwaki, "β-gallium oxide devices: Progress and outlook," Phys. Status Solidi RRL **15**, 2100357 (2021).
[6]A. J. Green, J. Speck, G. Xing, P. Moens, F. Allerstam, K. Gumaelius, T. Neyer, A. Arias-Purdue, V. Mehrotra, A. Kuramata, K. Sasaki, S. Watanabe, K. Koshi, J. Blevins, O. Bierwagen, S. Krishnamoorthy, K. Leedy, A. R. Arehart, A. T. Neal, S. Mou, S. A. Ringel, A. Kumar, A. Sharma, K. Ghosh, U. Singisetti, W. Li, K. Chabak, K. Liddy, A. Islam, S. Rajan, S. Graham, S. Choi, Z. Cheng, and M. Higashiwaki, "β-gallium oxide power electronics," APL Mater. **10**, 029201 (2022).
[7]L. E. Ratcliff, T. Oshima, F. Nippert, B. M. Janzen, E. Kluth, R. Goldhahn, M. Feneberg, P. Mazzolini, O. Bierwagen, C. Wouters, M. Nofal, M. Albrecht, J. E. N. Swallow, L. A. H. Jones, P. K. Thakur, T.-L. Lee, C. Kalha, C. Schlueter, T. D. Veal, J. B. Varley, M. R. Wagner, and A. Regoutz, "Tackling disorder in γ-Ga_2O_3," Adv. Mater. **34**, 2204217 (2022).
[8]J. García-Fernández, S. B. Kjeldby, P. D. Nguyen, O. B. Karlsen, L. Vines, and Ø Prytz, "Formation of γ-Ga_2O_3 by ion implantation: Polymorphic phase transformation of β-Ga_2O_3," Appl. Phys. Lett. **121**, 191601 (2022).
[9]H.-L. Huang, C. Chae, J. M. Johnson, A. Senckowski, S. Sharma, U. Singisetti, M. H. Wong, and J. Hwang, "Atomic scale defect formation and phase transformation in Si implanted β-Ga_2O_3," APL Mater. **11**, 061113 (2023).
[10]H.-L. Huang, J. M. Johnson, C. Chae, A. Senckowski, M. H. Wong, and J. Hwang, "Atomic scale mechanism of β to γ phase transformation in gallium oxide," Appl. Phys. Lett. **122**, 251602 (2023).
[11]J. Tang, K. Jiang, S. D. House, C. Xu, K. Xiao, L. M. Porter, and R. F. Davis, "Mg and Al-induced phase transformation and stabilization of Ga_2O_3-based γ-phase spinels," Appl. Phys. Lett. **123**, 012103 (2023).
[12]K. Jiang, J. Tang, C. Xu, K. Xiao, R. F. Davis, and L. M. Porter, "Evolution of β-Ga_2O_3 to γ-Ga_2O_3 solid-solution epitaxial films after high-temperature annealing," J. Vac. Sci. Technol. A **41**, 062702 (2023).
[13]J. Tang, K. Jiang, C. Xu, M. J. Cabral, K. Xiao, L. M. Porter, and R. F. Davis, "Atomic-scale investigation of γ-Ga_2O_3 deposited on $MgAl_2O_4$ and its relationship with β-Ga_2O_3," APL Mater. **12**, 011109 (2024).
[14]C. Wouters, M. Nofal, P. Mazzolini, J. Zhang, T. Remmele, A. Kwasniewski, O. Bierwagen, and M. Albrecht, "Unraveling the atomic mechanism of the disorder-order phase transition from γ-Ga_2O_3 to β-Ga_2O_3," APL Mater. **12**, 061113 (2024).
[15]J. García-Fernández, S. B. Kjeldby, L. J. Zeng, A. Azarov, A. Pokle, P. D. Nguyen, E. Olsson, L. Vines, A. Kuznetsov, and Ø Prytz, "In-situ atomic-resolution study of transformations in double polymorph γ/β-Ga_2O_3 structures," Mater. Adv. **5**, 3824–3831 (2024).

[16]A. Azarov, J. G. Fernández, J. Zhao, F. Djurabekova, H. He, R. He, Ø. Prytz, L. Vines, U. Bektas, P. Chekhonin, N. Klingner, G. Hlawacek, and A. Kuznetsov, "Universal radiation tolerant semiconductor," Nat. Commun. **14**, 4855 (2023).
[17]A. Y. Polyakov, A. A. Vasilev, A. I. Kochkova, I. V. Shchemerov, E. B. Yakimov, A. V. Miakonkikh, A. V. Chernykh, P. B. Lagov, Y. S. Pavlov, A. S. Doroshkevich, R. S. Isaev, A. A. Romanov, L. A. Alexanyan, N. Matros, A. Azarov, A. Kuznetsov, and S. J. Pearton, "Proton damage effects in double polymorph γ/β-Ga_2O_3 structures," J. Mater. Chem. C **12**, 1020–1029 (2024).
[18]M. Zinkevich, F. M. Morales, H. Nitsche, M. Ahrens, M. Rühle, and F. Aldinger, "Microstructural and thermodynamic study of γ-Ga_2O_3," Z. Metallkunde **95**, 756–762 (2004).
[19]H. Hayashi, R. Huang, H. Ikeno, F. Oba, S. Yoshioka, I. Tanaka, and S. Sonoda, "Room temperature ferromagnetism in Mn-doped γ-Ga_2O_3 with spinel structure," Appl. Phys. Lett. **89**, 181903 (2006).
[20]R. Huang, H. Hayashi, F. Oba, and I. Tanaka, "Microstructure of Mn-doped γ-Ga_2O_3 epitaxial film on sapphire (0001) with room temperature ferromagnetism," J. Appl. Phys. **101**, 063526 (2007).
[21]H. Hayashi, R. Huang, F. Oba, T. Hirayama, and I. Tanaka, "Epitaxial growth of Mn-doped γ-Ga_2O_3 on spinel substrate," J. Mater. Res. **26**, 578–583 (2011).
[22]H. Hayashi, R. Huang, F. Oba, T. Hirayama, and I. Tanaka, "Atomistic structure and energetics of interface between Mn-doped γ-Ga_2O_3 and $MgAl_2O_4$," J. Mater. Sci. **46**, 4169–4175 (2011).
[23]T. Oshima, Y. Kato, M. Oda, T. Hitora, and M. Kasu, "Epitaxial growth of γ-$(Al_xGa_{1-x})_2O_3$ alloy films for band-gap engineering," Appl. Phys. Express **10**, 051104 (2017).
[24]T. Oshima, K. Matsuyama, K. Yoshimatsu, and A. Ohtomo, "Conducting Si-doped γ-Ga_2O_3 epitaxial films grown by pulsed-laser deposition," J. Cryst. Growth **421**, 23–26 (2015).
[25]E. G. Víllora, K. Shimamura, Y. Yoshikawa, T. Ujiie, and K. Aoki, "Electrical conductivity and carrier concentration control in β-Ga_2O_3 by Si doping," Appl. Phys. Lett. **92**, 202120 (2008).
[26]E. A. Anber, D. Foley, A. C. Lang, J. Nathaniel, J. L. Hart, M. J. Tadjer, K. D. Hobart, S. Pearton, and M. L. Taheri, "Structural transition and recovery of Ge implanted β-Ga_2O_3," Appl. Phys. Lett. **117**, 152101 (2020).
[27]T. Yamanaka, Y. Takéuchi, and M. Tokonami, "Anharmonic thermal vibrations of atoms in $MgAl_2O_4$ spinel at temperatures up to 1933 K," Acta Crystallogr., Sect. B **40**, 96–102 (1984).
[28]R. D. Shannon, "Revised effective ionic radii and systematic studies of interatomic distances in halides and chalcogenides," Acta Crystallogr., Sect. A **32**, 751–767 (1976).
[29]O. Knacke, O. Kubaschweski, and K. Hesselmann, *Thermodynamical Properties of Inorganic Substances* (Springer, New York, 1991).
[30]S. Luo, G. F. Harrington, K.-T. Wu, and T. Lippert, "Heteroepitaxial (111) $ZnGa_2O_4$ thin films grown on (00.1) sapphire by pulsed laser deposition," Phys. Status Solidi RRL **14**, 2000270 (2020).
[31]S. Luo, L. Trefflich, S. Selle, R. Hildebrandt, E. Krüger, S. Lange, J. Yu, C. Sturm, M. Lorenz, H. von Wenckstern, C. Hagendorf, T. Höche, and M. Grundmann, "Ultrawide bandgap willemite-type Zn_2GeO_4 epitaxial thin films," Appl. Phys. Lett. **122**, 031601 (2023).
[32]M. Higashiwaki, K. Sasaki, A. Kuramata, T. Masui, and S. Yamakoshi, "Gallium oxide (Ga_2O_3) metal-semiconductor field-effect transistors on single-crystal β-Ga_2O_3 (010) substrates," Appl. Phys. Lett. **100**, 013504 (2012).
[33]G. A. Benesh and L. S. G. Liyanage, "The surface electronic structure of oxygen on Pt(00l)(1 × 1)," Surf. Sci. **261**, 207–216 (1992).
[34]P. R. Norton, P. E. Bindner, and K. Griffiths, "The adsorption of oxygen on Pt (100)-(1×1) and hex surfaces at 123 K," J. Vac. Sci. Technol. A. **2**, 1028–1031 (1984).
[35]G. N. Derry and P. N. Ross, "High coverage states of oxygen adsorbed on Pt (00l) and Pt(11l) surfaces," Surf. Sci. **140**, 165–180 (1984).
[36]C. Hou, R. M. Gazoni, R. J. Reeves, and M. W. Allen, "Direct comparison of plain and oxidized metal Schottky contacts on β-Ga_2O_3," Appl. Phys. Lett. **114**, 033502 (2019).
[37]A. M. Hyland, R. A. Makin, S. M. Durbin, and M. W. Allen, "Giant improvement in the rectifying performance of oxidized Schottky contacts to ZnO," J. Appl. Phys. **121**, 024501 (2017).
[38]J. Michel, D. Splith, J. Rombach, A. Papadogianni, T. Berthold, S. Krischok, M. Grundmann, O. Bierwagen, H. von Wenckstern, and M. Himmerlich, "Processing strategies for high-performance Schottky contacts on n-type oxide semiconductors: Insights from In_2O_3," ACS Appl. Mater. Interfaces **11**, 27073 (2019).
[39]A. Lajn, H. von Wenckstern, Z. Zhang, C. Czekalla, G. Biehne, J. Lenzner, H. Hochmuth, M. Lorenz, and M. Grundmann, "Properties of reactively sputtered Ag, Au, Pd, and Pt Schottky contacts on *n*-type ZnO," J. Vacuum Sci. Technol. B **27**, 1769–1773 (2009).
[40]S. Müller, H. von Wenckstern, F. Schmidt, D. Splith, H. Frenzel, and M. Grundmann, "Method of choice for the fabrication of high-quality β-gallium oxide-based Schottky diodes," Semicond. Sci. Technol. **32**, 065013 (2017).
[41]M. Kneiß, D. Splith, P. Schlupp, A. Hassa, H. von Wenckstern, M. Lorenz, and M. Grundmann, "Realization of highly rectifying Schottky barrier diodes and *pn* heterojunctions on κ-Ga_2O_3 by overcoming the conductivity anisotropy," J. Appl. Phys. **130**, 084502 (2021).
[42]S. Vogt, C. Petersen, H. von Wenckstern, M. Grundmann, T. Schultz, and N. Koch, "Zr doping in pulsed laser deposited α-Ga_2O_3 for device applications," Phys. Rev. Appl. **21**, 064016 (2024).
[43]D. A. Shirley, "High-resolution X-ray photoemission spectrum of the valence bands of gold," Phys. Rev. B **5**, 4709–4714 (1972).
[44]M. A. Moram and M. E. Vickers, "X-ray diffraction of III-nitrides," Rep. Prog. Phys. **72**, 036502 (2009).
[45]A. M. Miller, M. Lemon, M. A. Choffel, S. R. Rich, F. Harvel, and D. C. Johnson, "Extracting information from X-ray diffraction patterns containing laue oscillations," Z. Naturforsch. B **77**, 313–322 (2022).
[46]A. Glavic and M. Björck, "Genx 3: The latest generation of an established tool," J. Appl. Cryst. **55**, 1063–1071 (2022).
[47]E. Schierle, "Antiferromagnetism in thin films studied by resonant magnetic soft X-ray scattering," Doctoral Dissertation (Freie Universität Berlin, 2006).
[48]C. Ryang Wie, "High resolution X-ray diffraction characterization of semiconductor structures," Mater. Sci. Eng., R **13**, 1–56 (1994).
[49]B. P. Uberuaga, M. Tang, C. Jiang, J. A. Valdez, R. Smith, Y. Wang, and K. E. Sickafus, "Opposite correlations between cation disordering and amorphization resistance in spinels versus pyrochlores," Nat. Commun. **6**, 8750 (2015).
[50]A. Petitmangin, B. Gallas, C. Hebert, J. Perrière, L. Binet, P. Barboux, and X. Portier, "Characterization of oxygen deficient gallium oxide films grown by PLD," Appl. Surf. Sci. **278**, 153–157 (2013).
[51]A. I. Serykh and M. D. Amiridis, "In-situ X-ray photoelectron spectroscopy study of supported gallium oxide," Surf. Sci. **604**, 1002–1005 (2010).
[52]R. Carli and C. L. Bianchi, "XPS analysis of gallium oxides," Appl. Surf. Sci. **74**, 99–102 (1994).
[53]R. Carli, C. L. Bianchi, R. Giannantonio, and V. Ragaini, "Low temperature reduction of gallium in a Ga_2O_3/HZSM-5 catalyst," J. Mol. Catal. **83**, 379–389 (1993).
[54]D. Schmeisser, R. D. Schnell, A. Bogen, F. J. Himpsel, D. Rieger, G. Landgren, and J. F. Morar, "Surface oxidation states of germanium," Surf. Sci. **172**, 455–465 (1986).
[55]J. Oh and J. C. Campbell, "Thermal desorption of Ge native oxides and the loss of Ge from the surface," J. Electron. Mater. **33**, 364–367 (2004).
[56]S. Rafique, M. R. Karim, J. M. Johnson, J. Hwang, and H. Zhao, "LPCVD homoepitaxy of Si doped β-Ga_2O_3 thin films on (010) and (001) substrates," Appl. Phys. Lett. **112**, 052104 (2018).
[57]R. Sharma, M. E. Law, F. Ren, A. Y. Polyakov, and S. J. Pearton, "Diffusion of dopants and impurities in β-Ga_2O_3," J. Vac. Sci. Technol. A **39**, 060801 (2021).
[58]J.-S. Kim, M.-K. Joo, M. Xing Piao, S.-E. Ahn, Y.-H. Choi, H.-K. Jang, and G.-T. Kim, "Plasma treatment effect on charge carrier concentrations and surface traps in *a*-InGaZnO thin-film transistors," J. Appl. Phys. **115**, 114503 (2014).
[59]F. Schöppach, D. Splith, H. von Wenckstern, and M. Grundmann, "Oxygen plasma treatment to enable indium oxide MESFET devices," Adv. Electron. Mater. **9**, 2300291 (2023).